Non-shivering thermogenesis is intact upon brown-adipocyte specific loss of ATGL and HSL due to white adipose tissue browning

Yelina Manandhar[1], Anita Pirchheim[1], Peter Hofer[1], Nemanja Vujic[2], Dagmar Kolb[2,4], Gerald Hoefler[5], Dagmar Kratky[2,4], Martina Schweiger[1,4,6], Ulrike Taschler[1], Robert Zimmermann[1,4,6], Rudolf Zechner[1,4,6,*], and Renate Schreiber[1,7,*]

[1] University of Graz, Institute of Molecular Biosciences, NAWI Graz, 8010 Graz, Austria

[2] Medical University of Graz, Gottfried-Schatz Research Center, 8010 Graz, Austria

[3] Medical University of Graz, Center for Medical Research, Core Facility Ultrastructure Analysis, 8010 Graz, Austria

[4] BioTechMed-Graz, Austria

[5] Medical University of Graz, Diagnostic and Research Institute of Pathology, 8010 Graz, Austria

[6] BioHealth Graz

[7] Lead contact

*Correspondence to: renate.schreiber@uni-graz.at and rudolf.zechner@uni-graz.at

KEYWORDS

ATGL, HSL, lipolysis, non-shivering thermogenesis, brown adipose tissue, browning

Summary

Intracellular fatty acids (FAs) activate and fuel non-shivering thermogenesis (NST) mediated via uncoupling protein 1 (UCP1). Adipose triglyceride lipase (ATGL) and hormone-sensitive lipase (HSL) are the two main triacylglycerol lipases in adipocytes that control FA availability. We showed previously that a brown adipocyte-specific loss of ATGL does not affect cold-induced thermogenesis in brown adipose tissue (BAT) and NST, raising the question whether HSL-mediated FA release is sufficient to allow NST. Here, we show that a brown adipocyte-specific loss of both ATGL and HSL in mice leads to impaired BAT thermogenic capacity in cold, but still allows normal NST. The BAT defect is attributed to an impaired abundance of mitochondria as well as reduced oxidative capacity despite increased adipocyte numbers in BAT. Notably, the reduced thermogenesis in BAT of BAT-iDAKO mice leads to a concomitant upregulation of UCP1 expression (browning) in white adipose tissue (WAT) indicating that thermogenesis partially shifts from BAT towards WAT. In accordance with this assumption, genetic loss of ATGL and HSL in both BAT and WAT leads to dysfunctional BAT thermogenesis and defective browning in WAT resulting in blunted NST. Our study highlights the metabolic adaptability of adipose tissue and the critical role of intracellular lipolysis in the regulation of thermogenesis.

Introduction

Homeotherms maintain their body temperature within a narrow range upon variable ambient temperatures. Temperature homeostasis is preserved by different physiological processes including vasoconstriction, piloerection, and shivering. During cold exposure for several days to weeks (cold adaptation), however, mammals generate heat specifically in brown and beige adipocytes via non-shivering thermogenesis (NST), dissipating chemical energy as heat. NST is mainly mediated by uncoupling protein 1 (UCP1), enabling mitochondrial respiration without ATP synthesis. UCP1-independent NST may also occur by futile cycles of Ca^{2+}, creatine/phospho-creatine, or glycerol and fatty acids (FAs) - all of which depend on ATP[1,2]. NST is fueled by circulating glucose, FAs, and triglyceride-rich lipoproteins (TRLs)[3]. Thus, increased adipocyte thermogenesis is associated with improved glucose and lipid control and cardiometabolic health[4,5].

Despite its identification and purification in the early 1980s[6], the human UCP1 protein structure has been only reported recently[7]. The mechanism of UCP1 action, however, is still not fully understood[8–11]. A key step in UCP1-dependent NST is the activation of UCP1 by long-chain FAs[8,9,12–14]. These FAs are considered to derive from intracellular triacylglycerol (TG) breakdown (lipolysis)[15] mainly hydrolyzed by adipose triglyceride lipase (ATGL) and hormone-sensitive lipase (HSL)[16]. ATGL and HSL are indirectly or directly controlled by the sympathetic nervous system. Upon sensing cold, sympathetic nerve endings release catecholamines, which bind to β3-adrenergic receptors in brown adipocytes and initiate downstream signaling pathways to elevate cyclic AMP (cAMP) levels and activate protein kinase A (PKA). PKA in turn triggers several critical phosphorylation and translocation events of proteins involved in lipolysis[17–19] thus increasing FA release. PKA also controls the transcription of *Ucp1* and genes involved in adipocyte differentiation and mitochondrial biogenesis like *Pgc1α*, *Pppar*γ via p38/MAPK[20] and cAMP response element (CREB)[21,22]. Together, this coordinated response increases thermogenic capacity in brown adipocytes.

Loss of ATGL-mediated lipolysis in brown adipose tissue (BAT) challenged the dogma of this FA source being essential for NST[23,24]. In the absence of ATGL or its coactivator α/β hydrolase domain containing protein 5 (ABHD5, also known as CGI-58) in BAT, mice maintained euthermia in cold and showed normal NST raising the question as to „What ignites UCP1?“[25]. HSL cannot compensate for the loss of ATGL *in vivo* i.e. to provide fuel upon fasting[23,26] or to activate nuclear receptors[27]. However, HSL exhibits TG hydrolase activity *in vitro*[28] that may be sufficient to release FA for UCP1 activation for which the FA threshold is still unknown. Here we demonstrate that NST is intact despite the absence of both ATGL and HSL in BAT (BAT-iDAKO). On a molecular level, however, loss of ATGL and HSL attenuates the increase in BAT thermogenic capacity in cold due to low mitochondrial content despite

increased brown adipocyte number. Normal NST in BAT-iDAKO mice is enabled by increased thermogenic capacity of inguinal white adipose tissue (WAT). Accordingly, loss of ATGL and HSL in both BAT and WAT impairs thermogenic capacity in BAT and inguinal WAT thus disabling NST, but still allows the maintenance of euthermia in cold. Our study highlights the adaptability of adipose tissues and whole-body metabolism, and underscores the fundamental requirement of intracellular lipolysis in the regulation of thermogenesis.

Results

Genetic loss of ATGL and HSL in brown adipocytes leads to BAT hypertrophy. To study the loss of the two major adipocyte TG lipases ATGL and HSL, we generated *Pnpla2*$^{flx/flx}$*Lipe*$^{flx/flx}$::*Ucp1*-CreER$^{+/-}$ mice (synonym: BAT-iDAKO) to target tamoxifen-inducible gene deletion specifically in brown adipocytes (Figure 1A). Immunoblot analysis of whole BAT homogenates showed reduced protein levels of ATGL (-70%) and HSL (-84%) in BAT-iDAKO compared to *Pnpla2*$^{flx/flx}$*Lipe*$^{flx/flx}$ (synonym: ATGL$^{flx/flx}$HSL$^{flx/flx}$) littermate controls (Figure 1B). Enzyme activity assays in low-fat infranatants from BAT showed 60% lower TG hydrolase activities in BAT-iDAKO than in ATGL$^{flx/flx}$HSL$^{flx/flx}$ mice (Figure 1C). Addition of inhibitors specific for ATGL and HSL (ATGLi and HSLi, respectively) or the non-specific serine hydrolase inhibitor orlistat further reduced TG hydrolase activities in BAT samples from both genotypes. These data indicate residual active ATGL and HSL protein in the BAT of BAT-iDAKO mice. However, BAT of BAT-iDAKO mice was hypertrophic (Figure 1D, upper panel) with a ~5-fold increase in BAT mass (Figure 1E). Histological analysis revealed large and unilocular lipid droplets (LDs) throughout BAT sections of BAT-iDAKO mice compared to the characteristic multilocular LDs in BAT of ATGL$^{flx/flx}$HSL$^{flx/flx}$ mice (Figure 1D, lower panel). Taken together, these data show residual ATGL and HSL protein expression and TG hydrolase activities in BAT of BAT-iDAKO mice. However, BAT-iDAKO mice have a hypertrophic BAT with unilocular LDs, suggesting that the residual lipase expression likely derives from WAT that surrounds BAT.

BAT-iDAKO mice show increased body temperature and intact non-shivering thermogenesis upon cold adaptation. To assess the effect of BAT-specific ATGL and HSL deficiency on body temperature during cold exposure, we implanted telemetry devices to measure core body temperature (Figure 2A). BAT-iDAKO mice coped well with cold exposure and their core body temperature was +0.8 °C and +0.3 °C higher than in ATGL$^{flx/flx}$HSL$^{flx/flx}$ mice during day and night, respectively (Figure 2B). At room temperature (RT), core body temperature in BAT-iDAKO was +0.1 °C higher during the day and unchanged during night (Figure S1A) suggesting that the increase in body temperature is cold specific.

Analyses of body temperature do not allow an interpretation of functional non-shivering thermogenesis (NST). NST is facultative and adaptive, meaning it is activated only when needed, and its development is a long-term process taking weeks[22]. Therefore, we first acclimatized mice in cold for ≥3 weeks and tested the effect of the β3-adrenergic receptor agonist CL316,243 (CL) on whole-body O_2 consumption *in vivo* to assess NST[12,22]. Importantly, and similar to what was previously observed in mice lacking ATGL in BAT[23], BAT-iDAKO mice showed a comparable response in whole-body oxygen consumption (VO_2) to ATGL$^{flx/flx}$HSL$^{flx/flx}$ mice under unstimulated (basal) and CL-stimulated conditions (Figure 2C). Plasma FA and glycerol levels were also similar between genotypes (Figure 2D). These data demonstrate that brown adipocyte-specific ATGL- and HSL-mediated lipolysis is not required for NST.

To assess whether the BAT-specific loss of ATGL and HSL affects whole-body metabolism, we performed indirect calorimetry at 5 °C in cold-adapted mice. The respiratory exchange ratio (RER) was higher during the day and lower during the night in BAT-iDAKO than in ATGL$^{flx/flx}$HSL$^{flx/flx}$ mice (Figure S1B). These data indicate an attenuated light-induced switch from carbohydrate to fat combustion in BAT-iDAKO mice indicating reduced metabolic flexibility. Consistent with this, food intake was +32% higher in BAT-iDAKO mice during the day but unchanged at night (Figure S1C). Linear regression analyses of energy expenditure *vs* body weight - similar to ANCOVA[29] - revealed a trend towards higher EE during day in BAT-iDAKO mice, but not during the night (Figure S1D). Physical activity was unchanged between groups (Figure S1E). These data show that BAT-specific loss of ATGL and HSL causes a marked change in whole-body energy metabolism towards increased carbohydrate utilization.

BAT-iDAKO mice have impaired BAT thermogenic capacity upon cold adaptation. Normal whole-body respiration upon CL demonstrates an intact NST in BAT-iDAKO mice. Therfore, we next analyzed BAT of BAT-iDAKO mice in detail. Histology revealed a heterogenous cellular profile with brown adipocytes of different LD sizes, but also different cell types present in BAT sections from BAT-iDAKO mice as compared to the normal appearance in ATGL$^{flx/flx}$HSL$^{flx/flx}$ (Figure 3A, top). Gene expression analyses confirmed a marked fibrosis and inflammation in BAT of BAT-iDAKO mice during cold adaptation which was also present at RT (Figure S2A). Fibrinogen depositions in BAT of BAT-iDAKO were also visible in transmission electron microscopy images (TEM, Figure S2B). Similar to RT, immunoblot analyses showed a 90% reduction in ATGL and an 85% reduction in HSL protein expression, in BAT homogenates of BAT-iDAKO mice in cold (Figure S2C).

The thermogenic capacity of BAT was assessed by whole tissue UCP1 protein content, mitochondrial function, and substrate uptake analyses. Immunohistochemistry analyses showed low overall UCP1 protein expression in BAT sections of BAT-iDAKO mice (Figure 3A, bottom). To quantitate protein expression and thus whole BAT thermogenic capacity[30], tissue volume equivalents were loaded for immunoblot analyses to account for differences in BAT mass and cellular composition between genotypes. Immunoblot analyses confirmed low protein content of UCP1 (-66%) and other mitochondrial markers (≥60%) in BAT of BAT-iDAKO mice upon cold adaptation (Figure 3B). Remarkably, this difference in UCP1 and other mitochondrial proteins was not observed when mice were housed at RT (Figure S2D). Upon cold, BAT mass was ~3-fold higher in BAT-iDAKO than in ATGL$^{flx/flx}$HSL$^{flx/flx}$ mice (Figure 3C). Compared to RT (Figure 1E) and as expected, BAT mass increased by ~50% upon cold in ATGL$^{flx/flx}$HSL$^{flx/flx}$ mice suggesting brown adipocyte recruitment. In contrast, no difference in BAT mass was observed in BAT-iDAKO mice upon different ambient temperatures. Similar to the mitochondrial proteins, total protein content of the mitochondria-enriched fraction from the

entire BAT depot was unchanged between genotypes when mice were housed at RT, but 60% lower in BAT-iDAKO upon cold adaptation (Figure 3D). Concomitantly, mitochondrial respiration in BAT homogenates using glycerol-3-phosphate (G3P) as substrate was unchanged when mice were housed at RT, but 70% lower in cold adapted BAT-iDAKO than in ATGL$^{flx/flx}$HSL$^{flx/flx}$ mice (Figure 3E). Upon cold adaptation, ATGL$^{flx/flx}$HSL$^{flx/flx}$ mice showed the expected increase in respiration consistent with brown adipocyte recruitment. In contrast, BAT-iDAKO mice showed a similar respiration upon cold as at RT. Importantly, mitochondrial protein expression was not different in isolated mitochondria from BAT upon cold (Figure S2E). TEM analysis showed less mitochondria squeezed between LDs in BAT of BAT-iDAKO, but with intact and normal mitochondrial morphology (Figure S2B).

Next, we assessed whether impaired brown adipocyte recruitment causes low BAT capacity upon cold in BAT-iDAKO mice. Genes involved in brown adipocyte differentiation were similarly expressed in BAT of BAT-iDAKO and ATGL$^{flx/flx}$HSL$^{flx/flx}$ mice, but showed increased *Icam1* expression suggestive for higher number of adipocyte progenitors (Figure 3F). Next, we fractionated BAT into the stromavascluar fraction (SVF) and brown adipocytes (adi) from mice upon cold adaptation and isolated DNA as a measure of cell number. In line with elevated expression of inflammatory genes (Figure S2A), DNA content in isolated SVF was 6-fold higher in BAT-iDAKO (Figure 3G). Importantly, DNA content in the brown adipocyte fraction was 3.4-fold higher in BAT-iDAKO than in ATGL$^{flx/flx}$HSL$^{flx/flx}$ mice demonstrating brown adipocyte hyperplasia upon BAT-specific loss of ATGL and HSL. Finally, we assessed the relative mitochondrial content in the isolated brown adipocyte fractions showing that BAT-iDAKO mice have an abolished mitochondrial content (Figure 3H).

Although not a direct measure of BAT activity, but in line with reduced thermogenic capacity, radioactive tracer studies showed an attenuated energy substrate uptake of glucose (-70%), FA (-45%), and TRL-or LPL-mediated FA uptake (-35%) from TRLs in BAT of BAT-iDAKO upon cold adaptation (Figure 3I). Protein levels of GLUT1 were higher, but those of GLUT4 were lower in plasma membrane fractions from BAT of BAT-iDAKO (Figure S2F). Similarly, protein levels of the FA transporter CD36 were decreased in BAT-iDAKO BAT (Figure S2G). While LPL protein levels were higher in BAT of BAT-iDAKO mice, transcript levels of *Angptl4* - the LPL inhibitory protein - were 5-fold increased (Figure S2G-H). Reduced CD36 and increased *Angptl4* levels are consistent with the detected reduced FA uptake. In line with reduced BAT glucose uptake in BAT-iDAKO mice, expression of genes and proteins involved in *de-novo* lipogenesis was blunted (Figure S2I-J).

Together, these data suggest that mitochondria are *per se* intact in BAT-iDAKO. Upon cold adaptation, however, BAT-iDAKO are unable to adapt their BAT thermogenic capacity to environmental challenges.

Inguinal WAT (ingWAT) of BAT-iDAKO mice is browned upon cold adaptation. Intact NST despite impaired BAT capacity upon BAT-specific loss of ATGL and HSL prompted us to hypothesize whether WAT metabolism is affected to sustain NST. Indeed, UCP1 protein expression in ingWAT was 4-fold higher in BAT-iDAKO as shown by immunoblotting and IHC (Figure 4A-B). Protein levels of tyrosine hydroxylase (TH), the rate-limiting enzyme in catecholamine synthesis, were 3-times higher in ingWAT of BAT-iDAKO than in ATGL$^{flx/flx}$HSL$^{flx/flx}$ mice during cold (Figure 4A) indicative for an increased sympathetic tone. Functionally, mitochondrial respiration was 5-times higher in ingWAT homogenates of BAT-iDAKO than ATGL$^{flx/flx}$HSL$^{flx/flx}$ mice upon cold (Figure 4C). Inhibiting UCP1 by the addition of GDP resulted in 25% inhibition of respiration in ATGL$^{flx/flx}$HSL$^{flx/flx}$ and 50% reduction in BAT-iDAKO ingWAT confirming higher UCP1 activity in the latter. Energy substrate uptake was also higher for glucose (5.3-fold), FA (1.6-fold), and TRL (4.6-fold) in ingWAT of BAT-iDAKO mice (Figure 4D).

BAT-iDAKO mice harbor an estrogen receptor dependent Cre-recombinase (Cre) transgene under the transcriptional control of the UCP1 promotor (Ucp1-CreER). An increased UCP1 protein expression in ingWAT indicates Cre activity in this tissue, which would cause gene and protein deletion of *Pnpla2*/ATGL and *Lipe*/HSL. Indeed, gene expression analyses confirmed that Cre was substantially expressed in ingWAT of BAT-iDAKO during cold (Ct ~38 and ~27 for ATGL$^{flx/flx}$HSL$^{flx/flx}$ and BAT-iDAKO, respectively; Figure S3A). *Pnpla2* gene expression was not altered, but *Lipe* was 50% lower in ingWAT of BAT-iDAKO mice (Figure S3A). Similar results were obtained for ATGL and HSL protein expression (Figure S3B). Yet, these data did not translate into reduced lipolytic activities in bulk ingWAT homogenates of BAT-iDAKO mice (Figure S3C).

Collectively, our data suggest that enhanced β3-adrenergic signaling results in an increase in mitochondrial capacity in ingWAT of BAT-iDAKO mice during cold, driving fuel uptake and thermogenesis. Eventually, increased ingWAT browning may compensate for a dysfunctional BAT to maintain NST in BAT-iDAKO mice.

Genetic loss of ATGL and HSL in all adipocytes (DAKO) impairs NST upon cold adaptation. To assess the functional importance of ingWAT browning, we employed a mouse model with adipocyte-specific loss of ATGL and HSL (*Pnpla2*$^{flx/flx}$*Lipe*$^{flx/flx}$::AdipoQ-Cre$^{+/-}$; synonym: DAKO, Figure 5A). These mice lack ATGL and HSL protein as well as TG hydrolase activities in all adipose depots[31] (Figure S4A-B). While residual TG hydrolase activities in adipose tissue homogenates can be inhibited using the non-specific serine hydrolase inhibitor orlistat (Figure S4B), *in-vivo* lipolysis was not stimulated in DAKO mice compared to ATGL$^{flx/flx}$HSL$^{flx/flx}$ mice (Figure S4C). Collectively, these data demonstrate a complete loss of ATGL and HSL activity in adipose tissues of DAKO mice.

To assess thermogenic capacity in BAT of DAKO mice, protein expression analysis using tissue volume equivalents was performed. DAKO mice exhibited a substantial decrease in UCP1 protein content (-90%) and other mitochondrial marker proteins (≥70%, Figure 5B) in BAT homogenates. Concomitantly, BAT respiration and glucose uptake were blunted upon cold adaptation (Figure 5C-D). In contrast to BAT-iDAKO, UCP1 and other mitochondrial protein levels (Figure 5E), as well as respiration (Figure S4D) were blunted in ingWAT of DAKO mice. Accordingly, glucose uptake was lower in ingWAT of DAKO than in $ATGL^{flx/flx}HSL^{flx/flx}$ mice (Figure S4E). Importantly, and in contrast to BAT-iDAKO, cold-adapted DAKO mice showed no response to β3-adrenergic receptor activation using CL demonstrating impaired NST (Figure 5F).

Finally, to address the impact of blunted thermogenic capacity in both BAT and ingWAT on body temperature, we implanted telemetry transmitters and exposed mice to cold. Similar to BAT-iDAKO, DAKO maintained euthermia in the cold and exhibited +0.9 °C higher core body temperature during the day than $ATGL^{flx/flx}HSL^{flx/flx}$ mice (Figure 5G; left, time-course and right, mean). Similar to BAT-iDAKO (Figure S1), whole-body metabolism is markedly altered in DAKO mice. DAKO mice showed an attenuated switch of the RER between day and night indicative for impaired metabolic flexibility (Figure S4F). Food intake was 83% higher during day but unchanged during night (Figure S4G). In contrast to BAT-iDAKO, energy expenditure was lower during night periods along with attenuated physical activity (Figure S4H-I).

Taken together, these data demonstrate that DAKO mice exhibits dysfunctional BAT, abolished browning of ingWAT, and blunted NST. Yet, DAKO mice maintain euthermia which is associated with marked whole-body adaptations.

Discussion

FAs have important functions in UCP1-mediated thermogenesis: they deliver chemical energy and activate UCP1. Several in vitro studies have demonstrated that long-chain FAs activate brown adipocyte thermogenesis and UCP1 in particular[9,12–14]. In this regard, FAs derived from intracellular lipolysis have been considered to be essential[22,32], and a study in brown adipocytes and using small-molecule inhibitors showed that mitochondrial respiration largely depends on ATGL[33]. However, we and others showed that NST is intact in mice despite absent ATGL-mediated lipolysis in BAT[23,24]. Our studies suggested that WAT-derived FAs can sufficiently fuel BAT, but if true, would i) render β3-ARs in brown adipocytes meaningless or ii) suggest that UCP1 activator(s) other than FAs are released upon stimulation of β3-AR signaling[25]. ATGL and HSL are the two major lipases accounting for more than 90% of TG hydrolase activity in adipocytes[16] and non-adipocytes. While both lipases can hydrolyze TGs[28,34], but with different preference, HSL's TG hydrolase activity cannot compensate the loss of ATGL in WAT[26,35–37] or the heart[27] leading to fasting-induced hypometabolism and cardiomyopathy. In BAT, the threshold of FA levels needed to activate UCP1 is unknown, but it is feasible that HSL activity is sufficient to activate UCP1. Therefore, we assessed how a BAT-specific loss of both ATGL and HSL (BAT-iDAKO) affects NST.

Most importantly, BAT-iDAKO showed a normal whole-body respiratory response to the β3-AR agonist CL - a response depending on BAT[38,39] and UCP1[40,41]. These data demonstrate intact NST in the absence of neutral lipolysis in BAT. Recently, an alternative model lacking intracellular lipolysis-derived FAs in BAT was reported[42]. These mice lack the two main TG synthesizing enzymes acyl CoA:diacylglycerol acyltransferases DGAT1 and DGAT2, BAT is almost completely devoid of LDs, and thus lack the substrate for ATGL and HSL. These mice, however, showed a reduced whole-body response to CL indicative for attenuated NST. Reasons for the difference between these two mouse models may be i) a blunted FA release from WAT upon fasting in the DGAT knockout model and/or ii) secondary changes due to germline deletion *vs* inducible deletion in adult mice.

Remarkably, the loss of both ATGL and HSL impaired the thermogenic capacity of BAT upon cold adaptation suggesting that lipolysis is required to maintain a functional BAT upon high metabolic stress. Our data show that brown adipocyte recruitment is intact in BAT-iDAKO mice, but the mitochondrial content in these cells is abolished. Lipolysis is tightly intertwined with transcriptional regulation of G-protein coupled receptors[31] as well as PPARs[27,43–45] to control thermogenesis. Interestingly, the mitochondrial defect was not observed upon BAT-specific loss of ATGL[23] nor upon loss of DGAT1 and DGAT2[42] or whole-body b3-AR[46] - all of which have impaired intracellular lipolysis in BAT. BAT of UCP1-deficient mice exhibits a cold-induced mitochondrial failure[47,48]. This effect was not observed in BAT of BAT-iDAKO mice. Loss of ATGL and HSL has been implicated in the pathogenesis of

liposarcoma in BAT upon ageing[49]. We did not find clear evidence for a liposarcoma in BAT-iDAKO mice upon cold adaptation or when mice were allowed to age at least until 30 weeks of gene deletion at RT (data not shown) suggesting no benign cellular transformation upon loss of both ATGL and HSL in BAT under the conditions tested in this study.

Similar to other models of impaired BAT function[50], BAT-iDAKO mice showed a remarkable browning of inguinal WAT. Despite increased UCP1 and thus *Cre* expression, we observed no decrease in ATGL or HSL TG hydrolase activities in bulk tissue analyses. UCP1 IHC analyses indicate that different adipocyte subpopulations exist in inguinal WAT of BAT-iDAKO mice, but the lack of appropriate ATGL and HSL antibodies currently does not allow a co-staining with UCP1. Higher TH protein levels and markers of M2-like macrophages (not shown) indicate an increased sympathetic nerve activity causative for the browning effect[51–53]. Indeed, upon chemical denervation of inguinal WAT[54] and blocking downstream ATGL-mediated lipolysis[55], inguinal WAT browning was absent. In line, DAKO mice lacking ATGL and HSL in both BAT and WAT showed blunted UCP1 and mitochondrial protein levels. So, does inguinal WAT browning allow normal NST despite impaired BAT capacity in BAT-iDAKO mice? In DAKO mice with both fat depots being functionally impaired, NST was blunted similar as observed in whole-body β3-AR deficient mice[46,56]. These data suggest that inguinal WAT browning is essential to allow NST in mice upon loss of ATGL and HSL specifically in BAT.

Remarkably, we observed an increase in body temperature in both BAT-iDAKO and DAKO mice. Both models exhibit whole-body adaptations with an increased food intake during catabolic day periods. In addition, DAKO mice reduced energy expenditure due to lower physical activity during night possibly to spare energy. An increased glycerol/FA cycling in BAT[57] and WAT[47,58,59] has been suggested to contribute to thermogenesis compensating for the loss of UCP1. In both of our models, this glycerol/FA cycle is excluded in BAT of BAT-iDAKO as well as in BAT and WAT in DAKO mice due to the lipolytic defect. Whether other known futile cycles[60,61] contribute to thermoregulation in our models remains to be determined.

In summary, our data highlight that NST is intact in the absence of neutral lipolysis in brown adipocytes but the thermogenic capacity is shifted from BAT towards WAT.

STAR METHODS

Key resources table

REAGENT or RESOURCE	SOURCE	IDENTIFIER
Antibodies		
Adipose triglyceride lipase (ATGL)	Cell Signaling	Cat # 2138; RRID:AB_2167955
Hormone-sensitive lipase (HSL)	Cell Signaling	Cat # 4107; RRID:AB_2296900
Uncoupling protein 1 (UCP-1)	Abcam	Cat # ab10983; RRID:AB_2241462
NADH:ubiquinone oxidoreductase core subunit S1 (NDUFS1)	Abcam	Cat # ab157221; RRID:AB_2857900
Pyruvate dehydrogenase E1 alpha (PDHE1a)	Abcam	Cat # 177461; RRID:AB_2137173
Succinate dehydrogenase complex flavoprotein subunit A (SDHA)	Abcam	Cat # ab14715; RRID:AB_301433
Cytochrome c oxidase subunit 4 (COXIV)	Cell Signaling	Cat #4844; RRID: AB_2085427
Glucose transporter GLUT1	Cell Signaling	Cat #12939; RRID: AB_2687899
Glucose transporter GLUT4	Abcam	Cat #ab654; RRID: AB_305554
LPL	Gift from S.G. Young	
CD36	Abcam	Cat # ab133625; *RRID*:AB_2716564
Tyrosine hydroxylase (TH)	Millipore	Cat #MAB318; RRID:AB_2201528
Mitochondrially encoded cytochrome C oxidase 1 (MtCO1)	Abcam	Cat# ab14705 ; RRID :AB_204810
Acetyl-CoA carboxylase (ACC)	Cell Signaling	Cat# 3676; RRID:AB_2219397
Fatty acid synthase (FASN)	Cell Signaling	Cat# 3180; RRID:AB_2100796
VINCULIN	Sigma-Aldrich	Cat# V9131; RRID:AB_477629
GAPDH	Cell Signaling	Cat # 2118; RRID:AB_561053
Mouse-HRP	Sigma-Aldrich	Cat # NA931; RRID:AB_772210
Goat-HRP	Millipore	Cat # AP180P; RRID:AB_92573
Rabbit-HRP	Cell Signaling	Cat # 7074; RRID:AB_2099233
Chemicals, Peptides, and Recombinant Proteins		
Tamoxifen	Sigma-Aldrich	Cat #T5648
CL316,243	Sigma-Aldrich	Cat # C5976
Collagenase type 2	Sigma-Aldrich	Cat # C2-22
Dispase 2	Sigma-Aldrich	Cat # 04942078001
DNeasy® blood & tissue kit	Qiagen	Cat # 69504
Leupeptin	Roth	Cat # CN33.3
Antipain	Roth	Cat # 2933.2

REAGENT or RESOURCE	SOURCE	IDENTIFIER
Pepstatin	Roth	Cat # 2936.2
Protein Assay Dye	Bio-Rad	Cat # 500-0006
BCA Protein Assay	Pierce	Cat # 23225
PVDF membrane, 0.45 µm	Roth	Cat # T830.1
Clarity™ Western ECL Substrate	Bio-Rad	Cat # 170-5061
Phosphatidylcholine	Sigma-Aldrich	Cat # P3556
Phosphatidylinositiol	Sigma-Aldrich	Cat # P0639
BSA, essentially fatty acid free, 96%	Sigma-Aldrich	Cat # A6003
Triolein	Sigma-Aldrich	Cat # T7140
Atglistatin® (ATGLi)	Mayer et al., 2013	N/A
HSL inhibitor (HSLi)	Schweiger et al., 2006	N/A
Orlistat	Sigma-Aldrich	Cat # O4139
Triolein, [9,10-^{3}H(N)]	NEN Radiochemicals	Cat # NET431L
R-2-Br-palmitic acid, [1-^{14}C]	American Radiochemicals	Cat # ARC3623
Deoxy-D-glucose, 2-[1,2-3H (N)]	NEN Radiochemicals	Cat # NET328A250UC
Rotiszint eco plus	Roth	Cat # 0016.3
Solvable™	Solvable	Cat # 6NE9100
TRIzol™	Thermo Fisher Scientific	Cat # 15596018
Dnase I	NEB	Cat # M0303S
LunaScript RT SuperMix Kit	NEB	Cat # M3010X
Maxima SYBR Green, 2x	Fermentas, Thermo Fisher Scientific	Cat # K0223
Glycerol-3-phosphate, bis(cyclohexylammonium) salt (G3P)	Sigma-Aldrich	Cat # G7886
Cytochrome c	Sigma-Aldrich	Cat # C7752
Guanosine 5'-diphosphate, disodium salt (GDP)	Sigma-Aldrich	Cat # 51060
Antimycin A (Ama)	Sigma-Aldrich	Cat # A8674
NEFA-HR(2) R1 Set	Wako Chemicals	Cat # 434-91795
NEFA-HR(2) R2 Set	Wako Chemicals	Cat # 436-91995
Free glycerol reagent	Sigma-Aldrich	Cat # F6428
R/M-H extrudate	Ssniff	Cat # V1536-000
Oligonucleotides/Primers		
A full list of sequences is listed in Table S1	This paper	
Experimental Models: Organism / Strains // Synonym		
Mouse / *Pnpla2*$^{flx/flx}$ // ATGL$^{flx/flx}$	[63] The Jackson Laboratory	Cat # 024278
Mouse / *Lipe*$^{flx/flx}$ // HSL$^{flx/flx}$	[64] The Jackson Laboratory	Cat # 019004
Mouse / *Ucp1*-CreER$^{+/-}$	[65]	N/A
Mouse / *Adiponectin*-Cre	[66] The Jackson Laboratory	Cat # 010803
Mouse / *Pnpla2*$^{flx/flx}$*Lipe*$^{flx/flx}$ :: *Ucp1*-CreER$^{+/-}$ // BAT-iDAKO	This paper	
Mouse / *Pnpla2*$^{flx/flx}$*Lipe*$^{flx/flx}$ :: *Adiponectin*-Cre$^{+/-}$ // DAKO	This paper	N/A
Software		
Image Lab version 5.2.14	Bio-Rad	N/A
PhenoMaster Software	TSE	N/A
Dataquest™ A.R.T.™ version 4.31	DSI	N/A
DatLab version 5.1.1.91	OROBOROS® Instruments	N/A
GraphPad Prism 10.4.0	GraphPad	N/A
BioRender	BioRender.com	N/A

Resource availability

Lead contact. Further information and requests for resources, methods, and reagents should be directed to and will be fulfilled by the lead contact, Renate Schreiber (renate.schreiber@uni-graz.at).

Materials availability. Mouse models generated in this study are available from the lead contact, Renate Schreiber (renate.schreiber@uni-graz.at) upon completion of a material transfer agreement.

Data and code availability. This study did not generate any unique dataset or code.

Experimental model and subject details

Generation of mouse models

BAT-specific knockout models using Ucp1-Cre^{ER}. Tamoxifen-inducible BAT-specific double ATGL and HSL knockout mice (BAT-iDAKO) mice were generated by intercrossing *Pnpla2*$^{flx/flx}$ :: *Ucp1*-CreER$^{+/-}$ (iBAKO) with *Lipe*$^{flx/flx}$ mice (Haemmerle et al., 2002; The Jackson Laboratory stock number 019004) to obtain *Pnpla2*$^{flx/flx}$*Lipe*$^{flx/flx}$ :: *Ucp1*-CreER$^{+/-}$. *Pnpla2*$^{flx/flx}$*Lipe*$^{flx/flx}$ (ATGL$^{flx/flx}$HSL$^{flx/flx}$) littermates were used as controls. Tamoxifen-inducible BAT-specific single ATGL knockout mice (iBAKO; *Pnpla2*$^{flx/flx}$ :: *Ucp1*-CreER$^{+/-}$) mice were generated as described [23]. *Pnpla2*$^{flx/flx}$ (ATGL$^{flx/flx}$; The Jackson Laboratory stock number 024278) littermates were used as controls.

Adipocyte-specific knockout models using Adiponectin-Cre. Double adipocyte-specific ATGL and HSL knockout mice (DAKO) were generated by intercrossing *Pnpla2*$^{flx/flx}$ :: *Adiponectin*-Cre$^{+/-}$ mice with *Lipe*$^{flx/flx}$ mice to obtain *Pnpla2*$^{flx/flx}$*Lipe*$^{flx/flx}$ :: *Adiponectin*-Cre$^{+/-}$ mice. Adipocyte-specific HSL knockout mice (AHKO) were generated as described [67].

The expression of Cre recombinase, fused to the mutant form of the estrogen receptor (ER) ligand binding domain, and thus gene deletion was induced by oral gavage of 2 mg tamoxifen (Sigma-Aldrich, St. Louis, MO) solubilized in corn oil (Sigma) for five consecutive days. Both CreER$^{-/-}$ and CreER$^{+/-}$ mice obtained tamoxifen treatment at the age of at least 8 weeks. As indicated in the figure legends, studies were performed 6 – 11 weeks after the first tamoxifen administration. For cold adaptation, gene deletion was induced prior to cold exposure at 5 °C. To maintain gene deletion during cold adaptation and aging, an extended treatment strategy was applied and 2 mg tamoxifen per mouse were administered twice per week or once a month, respectively.

All mouse models were backcrossed onto a C57Bl/6J background for >10 generations, except otherwise stated. A summary of used mouse models is listed in the key resources table.

Mouse husbandry

All animal protocols were performed in accordance with the European Directive 2010/63/EU, the guidelines of the ethics committee of the University of Graz, and were approved by the Austrian Federal Ministry for Science, Research, and Economy (BMWF-66.007/0029-V/3b/2019). Experimental design and reporting for mouse studies follow the ARRIVE guidelines [68].

Mice were bred and maintained under specific pathogen free (SPF) conditions and fed a regular chow diet (R/M-H extrudate, V1536-000, Ssniff Spezialdiäten GmbH, Soest, Germany). Health status of mice was monitored according to the guidelines of the Federation of European Laboratory Animal Science Associations (FELASA) three times per year using the dirty bedding sentinel program. Regular housing temperatures were maintained between 22-23 °C with a 14 h light / 10 h dark cycle. If possible, mice were maintained in groups with 2-4 mice per cage during maintainance and had *ad libitum* access to water and regular chow diet. After completion of animal protocols, blood was collected via the retro-orbital sinus, mice were euthanized by cervical dislocation, tissues were dissected and immediately processed or flash-frozen in liquid N_2. Plasma and tissue samples were stored at -80 °C until further analyses.

For all studies, age-matched male littermates were used as controls. Genotype, sex, age, time upon tamoxifen treatment, and number of mice are indicated for each experiment in the appropriate figure legends. Mice were allocated to experimental groups based on their genotype and were treatment-naïve at the time of the study, except for inducible mutant mice receiving tamoxifen treatment.

Studies at cold

For cold adaptation studies, mice were single-housed and transferred from 22-23 °C to 5 °C for ≥3 weeks. Mice had free access to food and water.

Analyses of body temperature

Body temperature was assessed in conscious mice using a rectal probe RET-3 (Physitemp, Clifton, NJ). Core body temperature (CBT) was studied using implantable telemetry devices (TA-F10, Data Sciences International, DSI, St. Paul, MN). Telemetry devices were surgically implanted in anesthetized mice (95 µg ketamine and 9,5 µg xylazine per g body weight). Upon surgery, mice were kept on heating plates at 37 °C until they regained consciousness, and were single-housed post-surgery to avoid interference during measurements. Animals received 0.1 mg enrofloxacin and 2 mg ibuprofen per ml drinking water for 3-4 days. Together, mice were allowed to recover from surgery for 7-10 days. CBT was continuously assessed at an interval of 2 min for a period as indicated. Data acquisition and analyses were performed using Dataquest™ A.R.T.™ software (version 4.31; DSI).

Metabolic phenotyping

Oxygen consumption, carbon dioxide production, respiratory exchange ratio (RER), energy expenditure, and locomotor activity were analyzed at given ambient temperatures in unrestrained mice using a laboratory animal monitoring system supplemented with an ActiMot module (PhenoMaster, TSE Systems GmbH, Bad Homburg, Germany). Mice were familiarized to single housing and drinking flasks for ≥24 h before metabolic phenotyping. Then, experiments were performed for four consecutive days. Data of the first recorded 12 h were excluded from all analyses. Data were separated on the basis of regular light and dark cycle, averaged or summed up (locomotor activity) of indicated time periods, and analyzed according to guidelines[69]. Food intake was determined manually by weighing the food from single-housed mice every day at 9 AM and 6 PM representing dark and light periods, respectively.

Analyses of non-shivering thermogenesis

To test the non-shivering thermogenic (NST) capacity, the metabolic rate upon administration of the β_3-adrenoreceptor agonist CL316,243 (CL; Sigma) was monitored using PhenoMaster (TSE). Mice were anesthetized with pentobarbital (75 mg per kg body weight, *i.p*. injection), which does not inhibit NST [70,71]. Basal metabolic rate was monitored for subsequent 30 min until reaching steady-state. Then, CL was injected *i.p*. using a dosage of 1 mg CL per kg body weight. The subsequent increase in metabolic rate was monitored for 60-80 min. Metabolic rates were measured at an ambient temperature of ~30°C [71]. Control and knockout mice were analyzed in parallel in an interval of 2 min (1 min per cage). Data were analyzed using PhenoMaster Sofware and are expressed as VO_2 (ml/h).

Metabolic tracer studies

To trace glucose uptake, 10 µCi of 2-[1,2-^{3}H (N)]-deoxy-D-glucose (NEN) were i.v. injected to *ad libitum* fed mice. To trace FAs, [1-^{14}C]-*R*-2-Br-palmitic acid (American Radiolabeled Chemicals) was complexed in a saline solution containing 1% BSA (Sigma). Radioactively labelled TG rich lipoproteins (TRL) particles were prepared as described with minor modifications [72,73]. Briefly, TRL-like particles were prepared from 34.2 mg of total lipid including 25.2 mg TO (Sigma), 8.172mg phosphatidylcholine (Sigma), 0.828 mg lysophosphatidylcholine (Sigma) supplemented with 36 µCi ^{3}H-TO (NET431L, NEN). Lipids were dried and sonicated in 3.6 ml of phosphate-buffered saline (Virsonic 475, Virtis, Gardiner, NJ) to produce TRL-like particles. Prior to FA and TRL tracer experiments, mice were fasted for 2 h in cold. Then, mice were i.v injected via the retroorbital sinus with 100 µl saline solution containing 1 µCi *R*-2-Br-palmitic acid or 2 µCi ^{3}H-TRL particles. Upon 15 min of tracer administration and in cold, blood was collected, mice were euthanized and tissues were dissected and stored at -20°C until further analyses. To determine radioactivity, an aliquot of total tissue was weighed and lysed overnight in

0.5-1 ml Solvable™ (Solvable) based on tissue weight at 55 °C with constant shaking. Aliquots of 200 µl of tissue lysates were added to 5 ml of scintillation cocktail (Rotiszint) and the radioactivity was analyzed using liquid scintillation counting (HIDEX 600 SL; Hidex Germany Sales GmbH). The radioactivity was calculated per total tissue.

In vivo lipolysis

To assess whole body lipolysis, blood was collected in the ad libitum fed (basal) state and 15 min post-CL injection (i.p.). As a readout for lipolysis, plasma FA (NEFA-HR, Wako Chemicals) and plasma glycerol (free glycerol reagent, Sigma) concentrations were quantified using enzymatic colorimetric methods following manufacturer's instructions.

Histological analyses

Fat tissues were fixed in 4% buffered formaldehyde and embedded in paraffin. Prior to hematotoxylin/eosin (H/E) or immunohistochemistry (IHC), 2 µM cut sections were deparaffinized using xylene, and rehydrated using descending dilutions of ethanol and distilled water. For H/E staining, the sections were then stained with hematoxylin. After washing, the sections were stained with eosin-phloxin and dehydrated with ethanol. Thereafter, the sections were cleared using butylacetate, mounted, and visualized. For IHC, sections were placed in EDTA Na buffer (0.5 M/pH: 8) and heated for 40 min at 150 W in a microwave for antigen retrieval. After cooling, the sections were washed using distilled water and phosphate-buffered saline, and blocked using 3% H_2O_2 in methanol for 15 min at RT to block endogenous peroxidase activity. Thereafter, the slides were incubated with primary antibodies against UCP1 (1:100 dilution in Abcam 10983 in Dako antibody diluent) for 60 min at RT. Slides were then incubated with EnVision™ Dual Link System-HRP (# K5007, DAKO, Agilent Technologies, Santa Clara, CA) for 30 min at RT and visualized using the AEC Substrate Chromogen (#958D-20, Cell Marque). Upon washing, slides were counter-stained with haematotoxylin to stain nuclei, mounted with aquatex (Merck), and visualized.

Transmission electron microscopy

Mice were anesthetized using 258 mg ketamine and 25.8 mg xylazine per g body weight. After ensuring deep anesthesia, mice were perfused with ice-cold phosphate-buffered saline, and subsequently with 4% paraformaldehyde. Then, BAT was dissected and cut into small fragments, and fixed in 2.5% (w/v) glutaraldehyde and 2% (w/v) paraformaldehyde in 0.1 M cacodylate buffer at pH: 7.4 for 3 h, post-fixed in 2% (w/v) osmium tetroxide for 3 h at RT. After dehydration in graded series of ethanol, tissues were infiltrated (ethanol and TAAB epoxy resin, pure TAAB epoxy resin) and placed in TAAB epoxy resin for 8 h, transferred into embedding moulds, and polymerized for 48 h at 60 °C. Ultrathin sections of 70 nm were cut with a UC 7 Ultramicrotome (Leica Microsystems, Vienna, Austria) and stained with

lead citrate for 5 min and platin blue for 15 min. Electron micrographs were taken using a Tecnai G2 transmission electron microscope (FEI, Eindhoven, Netherlands) with a Gatan ultrascan 1000 charge coupled device (CCD) camera (−20 °C; acquisition software Digital Micrograph; Gatan, Munich, Germany). Acceleration voltage was 120 kV. Further investigations were made with the scanning electron microscope. The Scanning transmission electron microscopy mode (STEM) of a field emission scanning electron microscope (ZEISS FE-SEM Sigma 500) in combination with ATLAS TM was used to perform imaging on large areas of BAT with high resolution.

Analyses of gene expression and relative mitochondrial content using RT-qPCR

Total RNA was extracted from snap-frozen tissues using TRIzol™ reagent following manufacturer's instruction (Invitrogen). The quality of RNA was verified by standard agarose gel electrophoresis. RNA concentrations were analyzed using NanoDrop® microvolume spectrophotometer (Thermo Fisher Scientific). To avoid DNA contaminations, 1 µg RNA were digested with 1U Dnase I (NEB, Thermo Fisher Scientific) at 37 °C for 10 min followed by addition of 1 µl 50 mM EDTA and heat inactivation of the enzyme at 75 °C for 10 min. Thereafter, 1 µg RNA was transcripted into single-strand cDNA using LunaScript RT SuperMix Kit (NEB, Thermo Fisher Scientific). For gene expression or relative mitochondrial content, 8-40 ng cDNA were used for the PCR reaction using 10 pmol of forward and reverse primers, SYBR Green technology (Fermentas, Thermo Fisher Scientific), and StepOnePlus™ Real-Time PCR System (Thermo Fisher Scientific). Relative gene expression and mitochondrial content were analyzed using the ΔΔ-Ct method [74]. Relative gene expression was normalized to *Tbp, 36b4, or AdipoQ* (to account for adipocyte-specific gene expression). Relative mtDNA content was determined as ratio of the copy numbers from the mtDNA encoded gene (MtCO1) to the nuclear DNA encoded gene (Ndufv1). A list of gene-specific primers is available in Table S1.

Fractionation of BAT (adipocytes, stromavascular fraction) and DNA isolation

Freshly dissected BAT depots were freed from WAT. Whole BAT depots were cut into small pieces and digested as previously described[23] using collagenase 2 and dispase 2 (both Sigma). Subsequently, DNA was isolated from isolated brown adipocytes and the stromavascular fraction (SVF) using the DNeasy blood & tissue kit (Qiagen, Hilden, Germany). DNA concentration was determined by NanoDrop spectrophotometer (Thermo Fisher Scientific).

Isolation of different cellular fractions from BAT (mitochondria/lysosomes, plasma membrane)

For the enrichment of mitochondria, BAT depots were cut into small pieces and homogenized in ice-cold solution A (0.25 M sucrose, 1 mM EDTA, 1 mM dithiothreitol, pH: 7.0 supplemented with 20 µg/ml leupeptin, 2 µg/ml antipain, 1 µg/ml pepstatin; Carl Roth GmbH & Co KG, Karlsruhe, Germany), filtered through a 100 µm cell strainer, and centrifuged at 1,000 x *g* for 10 min and 4 °C. Pellets containing

nuclei and unbroken cells were discarded. The supernatant excluding floating fat was collected and centrifuged at 12,000 x *g* for 30 min and 4 °C. This supernatant was discarded and pellets containing mitochondria were washed twice in ice-cold solution A and centrifuged at 12,000 x *g* for 15 min and 4 °C. The pellets were resuspended in solution A and the protein content was analyzed using Protein Assay Dye (Bio-Rad) and BSA as standard.

For the isolation of plasma membrane, BAT depots were cut into small pieces and homogenized in an ice-cold Tris-sucrose buffer (50 mM Tris-Cl, 250 mM sucrose, pH: 7.4). The cut tissue pieces were homogenized in a pre-cooled Dounce homogenizer using 15 strokes. Collected tissue homogenates were filtered through a 100 µm cell strainer and centrifuged at 800 x *g* for 10 min and 4 °C. The pellet, containing nuclei and unbroken cells, was discarded. The supernatant was collected and centrifuged at 16,000 x *g* for 30 min and 4 °C to pellet mitochondria. Then, the resulting supernatant excluding the floating fat and the mitochondria pellet was centrifuged at 100,000 x *g* (Beckman Optima™ TLX Ultracentrifuge) for 2 h at 4 °C. The supernatant containing the cytosol fraction was collected and the pellet containing the plasma membrane fraction was resuspended in Tris-sucrose buffer by sonicating in water bath for 15 min. The resuspended pellets were re-centrifuged at 100,000 x *g* for 45 min at 4 °C. The pellets were resuspended in Tris-sucrose buffer using 15 min of sonication in a water bath, followed by several passes through a 26-gauge needle. The protein content was analyzed using Protein Assay Dye (Bio-Rad) and BSA as standard.

Immunoblotting

For BAT and ingWAT, one depot was weighed and homogenized in ice-cold solution A using Ultra-Turrax® Homogenizer (IKA, Staufen, Germany). One tissue depot was lysed in a respective volume to adjust to a final volume of 1 ml taking into account the volume changes due to the tissue mass increase. The homogenates were filtered through a 100 µm cell strainer to get rid of connective tissue. For delipidation, homogenates were processed according to Wessel and Flügge[75] with minor modifications. In brief, 40 µl of tissue homogenate was mixed with 140 µl water. Then, 800 µl of methanol and 200 µl chloroform were added to the homogenate and vortexed vigorously. An additional 600 µl water was added to facilitate phase separation and vortexed vigorously. Samples were centrifuged at 12,500 x *g* for 5 min and RT. The upper aqueous phase was removed and 600 µl methanol was added to the remaining lower phase. Samples were centrifuged, the supernatant was removed, and the protein pellet was air-dried, lysed in 80 µl of SDS sample buffer, and denatured. Tissue homogenates equivalent to 0.25% of total tissue were loaded onto a SDS polyacrylamide gel.

Alternatively, adipose depots were homogenized in ice-cold RIPA lysis buffer (150 mM NaCl, 10 mM Tris-HCl pH: 7.4, 0.1% SDS, 1% Triton X-100, 1% sodium deoxycholate, and 5 mM EDTA pH: 8.0, supplemented with 20 µg/ml leupeptin, 2 µg/ml antipain, 1 µg/ml pepstatin, and phosphatase inhibitor

cocktail (PhosSTOP, Roche) using Ultra-Turrax® and filtered through a 100 µm cell strainer. Samples were centrifuged at 12,000 x g for 30 min and 4 °C, the infranatant excluding the fat layer was collected, and protein content was determined using BCA assay (Pierce BCA Protein Assay Kit, Thermo Scientific) and BSA as standard. Protein samples of 1-20 µg were solubilized, denatured in SDS sample buffer, and loaded onto a SDS polyacrylamide gel.

Proteins were resolved by SDS-PAGE using a 10 or 12.5% SDS polyacrylamide gel, transferred onto a polyvinylidene fluoride (PVDF) transfer membrane (Roth) in CAPS buffer (10 mM CAPS, 10% methanol, pH: 11.0). The membranes were blocked with blocking buffer using 10% blotting grade milk powder (Roth) in TST (50 mM Tris-HCl, 0.15 M NaCl, 0.1% Tween-20, pH: 7.4) for ≥1 h at RT or overnight at 4 °C. Antibodies are listed in the Key Resources Table. Protein expression was visualized by enhanced chemiluminescence using Clarity™ Western ECL Substrate and ChemiDoc™ Touch Imaging System (Bio-Rad). Signal intensities were quantified by densitometric analyses using Image Lab version 5.2.1 Software (Bio-Rad). Total protein stain was performed using Coomassie stain solution for a few seconds and subsequent washing steps in de-staining solution.

In-vitro enzyme activity assays

Low fat tissue homogenates were prepared in solution A and centrifuged at 20,000 x *g* for 30 min at 4 °C to obtain low-fat tissue infranatants. TG hydrolase activities were assessed as described[76]. The TG substrate consisted of 1.67 mM triolein (Sigma) and 188 µM PC:PI (3:1; Sigma) supplemented with ~1,5 x 10^3 cpm/nmol triolein [9,10-^{3}H(N)] (NET431L, NEN Radiochemicals) per reaction. Lipids were mixed, dried under a N_2 stream, and emulsified by sonication (Virsonic 475) on ice in 100 mM potassium phosphate buffer at pH: 7.0. Then, substrates were adjusted to 5% FA-free BSA (Sigma) and kept on ice until usage. Lipolytic activities were inhibited using small-molecule inhibitors specific for ATGL (Atglistatin®, ATGLi; final concentration: 40 µM[62]), HSL (HSLi; final concentration: 10 µM; NovoNordisk, Copenhagen, DK;[16]), or using the non-specific serine hydrolase inhibitor orlistat (final concentration: 10 µM). Control incubations contained DMSO.

To determine neutral TG hydrolase activities, 25 µl of the substrate were mixed with 20-50 µg sample to obtain a final volume of 50 µl. As blank, 25 µl solution A were incubated under the same conditions as samples. The reaction mixtures were incubated in a water bath at 37 °C for 1 h. Then, 650 µl of methanol/chloroform/heptane (10/9/7, v/v/v) and 200 µl of 0.1 M potassium-carbonate/0.1 M boric acid (pH: 10.5) were added to terminate the reaction. The reaction mixture was intensively vortexed and centrifuged for 10 min at 800 x *g*. An aliquot of 200 µl of the upper aqueous phase was collected in 2 ml scintillation cocktail (Rotiszint eco plus, Roth) and the radioactivity was analyzed using liquid scintillation counting (Tri-Carb 2100TR, Packard Instrument Company, Downers Grove, IL). Corrections for background were accounted using counts obtained for blank incubation. Samples from control and

mutant mice were run in parallel and analyzed in triplicates or quadruplets. TG hydrolase activities were expressed as released FA per h and normalized to mg tissue protein.

Analyses of oxygen consumption rates

Freshly dissected BAT (freed from WAT) and ingWAT depots were collected, minced into small pieces, and homogenized in ice-cold 250 mM sucrose solution in a total volume of 1 ml for 2-3 s using Ultra-Turrax® Homogenizer. Prior to the analyses, homogenates were freed from connective using a 100 µm cell strainer. Oxygen consumption rates were measured at 37 °C using polarographic oxygen sensors in a two-chamber Oxygraph (OROBOROS® Instruments, Innsbruck, Austria). A tissue volume equivalent of 20-100 µl (total volume = 1 ml per ½ tissue depot) was incubated in respiration buffer containing 125 mM sucrose, 20 mM potassium TES buffer (pH: 7.2), 2 mM $MgCl_2$, 1 mM EDTA, 4 mM KH_2PO_4, 3 mM malate, and 0.1% FA-free BSA (Sigma). Respiration was analyzed by the following protocol adding substrates sequentially upon reaching steady-state: 5 mM glycerol-3-phosphate (G3P; complex-II) and 10 µM cytochrome c, and 2 mM guanosine 5-diphosphate (GDP, dissolved in 20 mM TES buffer pH: 7.2), and 2.5 µM antimycin a (Ama). Substrates and inhibitors were prepared according to Oroboros O2k protocols. Data acquisition and analyses were performed using DatLab. Analyses of control and mutant mice were prepared and run in parallel. Tissue respiration rates using tissue homogenates were calculated for whole depot per mouse and were expressed as nmol/min/entire depot.

Quantification and statistical analyses

Figures were prepared using GraphPad Prism 10.4.0 software (GraphPad Software, San Diego, CA). All data are shown as means + S.D. except otherwise stated. In each experiment, *n* defines the number of mice. Statistical significance between two groups was determined by unpaired, two-tailed Student's *t*-test. Simple linear regression analyses were used to assess differences between slope elevations. Group differences were considered statistically different for *, $p<0.05$, **, $p<0.01$, and ***, $p<0.001$. Statistical tests, exact values of *n*, definitions of center, dispersion, and significance are indicated in the figure legends.

Acknowledgements

We thank Wolfgang Krispel, Sabrina Hütter, and Silvia Schauer for excellent technical assistance. Kathrin A. Zierler and her team for excellent animal care and genotyping. This work was supported by the PhD training program doc.fund „Molecular Metabolism-MOBILES“ 10.55776/DOC50 (R. Zimmermann, R. Zechner), 10.55776/PAT3403323 (U.T.), and the SFB „Lipid Hydrolysis“ 10.55776/F73 (D. Kr., R. Zi./U. T., R. Ze./R.S.) funded by the Austrian Science Fund FWF, the Leducq Foundation Grant 12CVD04, and the Louis Jeantet Foundation. R.S. and M.S. are grateful to the Austrian Science Fund FWF for excellence cluster 10.55776/COE14. For the purpose of open access, the authors have applied a CC BY public copyright license to any author accepted manuscript version arising from this submission. We thank the University of Graz for financial support and gratefully acknowledge the support of NAWI Graz, BioTechMed-Graz, and the *Field of Excellence* BioHealth-University of Graz, Graz, Austria.

Author contributions

R.S. and R.Ze. conceptualized the study. M.Y. and R.S. conducted most of the experiments and analyzed data. A.P. and P.H. performed immunoblotting and activity assays. D.Ko. and G.H. analyzed electron microscopy and histological analyses, respectively. N.V. and D.Kr. provided indirect calorimetry devices. M.Y. and R.S. wrote the manuscript, M.Y., M.S., U.T., R.Zi., R.Ze., and R.S. reviewed and edited the manuscript.

References

1. Sharma, A.K., Khandelwal, R., and Wolfrum, C. (2024). Futile lipid cycling: from biochemistry to physiology. Nat. Metab. *6*, 808–824. https://doi.org/10.1038/s42255-024-01003-0.

2. Cohen, P., and Kajimura, S. (2021). The cellular and functional complexity of thermogenic fat. Nat. Rev. Mol. Cell Biol. *22*, 393–409. https://doi.org/10.1038/s41580-021-00350-0.

3. Heine, M., Fischer, A.W., Schlein, C., Jung, C., Straub, L.G., Gottschling, K., Mangels, N., Yuan, Y., Nilsson, S.K., Liebscher, G., et al. (2018). Lipolysis triggers a systemic insulin response essential for efficient energy replenishment of activated brown adipose tissue in mice. Cell Metab. *28*, 644–655. https://doi.org/10.1016/j.cmet.2018.06.020.

4. Becher, T., Palanisamy, S., Kramer, D.J., Eljalby, M., Marx, S.J., Wibmer, A.G., Butler, S.D., Jiang, C.S., Vaughan, R., Schöder, H., et al. (2021). Brown adipose tissue is associated with cardiometabolic health. Nat. Med. *27*, 58–65. https://doi.org/10.1038/s41591-020-1126-7.

5. Bartelt, A., Bruns, O.T., Reimer, R., Hohenberg, H., Ittrich, H., Peldschus, K., Kaul, M.G., Tromsdorf, U.I., Weller, H., Waurisch, C., et al. (2011). Brown adipose tissue activity controls triglyceride clearance. Nat. Med. *17*, 200–206. https://doi.org/10.1038/nm.2297.

6. Lin, C.S., and Klingenberg, M. (1980). Isolation of the uncoupling protein from brown adipose tissue mitochondria. FEBS Lett. *113*, 299–303. https://doi.org/10.1016/0014-5793(80)80613-2.

7. Kang, Y., and Chen, L. (2023). Structural basis for the binding of DNP and purine nucleotides onto UCP1. Nature *620*, 226–231. https://doi.org/10.1038/s41586-023-06332-w.

8. Fedorenko, A., Lishko, P. V., and Kirichok, Y. (2012). Mechanism of fatty-acid-dependent UCP1 uncoupling in brown fat mitochondria. Cell *151*, 400–413. https://doi.org/10.1016/j.cell.2012.09.010.

9. Winkler, E., and Klingenberg, M. (1994). Effect of fatty acids on H+ transport activity of the reconstituted uncoupling protein. J. Biol. Chem. *269*, 2508–2515.

10. Skulachev, V.P. (1991). Fatty acid circuit as a physiological mechanism of uncoupling of

oxidative phosphorylation. FEBS Lett. *294*, 158–162. https://doi.org/10.1016/0014-5793(91)80658-p.

11. Garlid, K.D., Orosz, D.E., Modrianský, M., Vassanelli, S., and Ježek, P. (1996). On the mechanism of fatty acid-induced proton transport by mitochondrial uncoupling protein. J. Biol. Chem. *271*, 2615–2620. https://doi.org/10.1074/jbc.271.5.2615.

12. Prusiner, S.B., Cannon, B., Ching, T.M., and Lindberg, O. (1968). Oxidative Metabolism in Cells Isolated from Brown Adipose Tissue. Eur. J. Biochem. *7*, 51–57. https://doi.org/10.1111/j.1432-1033.1968.tb19572.x.

13. Bukowiecki, L.J., Folléa, N., Lupien, J., and Paradis, A. (1981). Metabolic relationships between lipolysis and respiration in rat brown adipocytes. The role of long chain fatty acids as regulators of mitochondrial respiration and feedback inhibitors of lipolysis. J. Biol. Chem. *256*, 12840–12848.

14. Locke, R.M., Rial, E., Scott, I.D., and Nicholls, D.G. (1982). Fatty acids as acute regulators of the proton conductance of hamster brown-fat mitochondria. Eur. J. Biochem. *129*, 373–380. https://doi.org/10.1111/j.1432-1033.1982.tb07060.x.

15. Grabner, G.F., Xie, H., Schweiger, M., and Zechner, R. (2021). Lipolysis: cellular mechanisms for lipid mobilization from fat stores. Nat. Metab. *3*, 1445–1465. https://doi.org/10.1038/s42255-021-00493-6.

16. Schweiger, M., Schreiber, R., Haemmerle, G., Lass, A., Fledelius, C., Jacobsen, P., Tornqvist, H., Zechner, R., and Zimmermann, R. (2006). Adipose triglyceride lipase and hormone-sensitive lipase are the major enzymes in adipose tissue triacylglycerol catabolism. J. Biol. Chem. *281*, 40236–40241. https://doi.org/10.1074/jbc.M608048200.

17. Granneman, J.G., Moore, H.P.H., Krishnamoorthy, R., and Rathod, M. (2009). Perilipin controls lipolysis by regulating the interactions of AB-hydrolase containing 5 (Abhd5) and adipose triglyceride lipase (Atgl). J. Biol. Chem. *284*, 34538–34544. https://doi.org/10.1074/jbc.M109.068478.

18. Miyoshi, H., Perfield, J.W., Souza, S.C., Shen, W.J., Zhang, H.H., Stancheva, Z.S., Kraemer, F.B., Obin, M.S., and Greenberg, A.S. (2007). Control of adipose triglyceride lipase action by serine

517 of perilipin A globally regulates protein kinase a-stimulated lipolysis in adipocytes. J. Biol. Chem. *282*, 996–1002. https://doi.org/10.1074/jbc.M605770200.

19. Yang, X., Lu, X., Lombès, M., Rha, G.B., Chi, Y.I., Guerin, T.M., Smart, E.J., and Liu, J. (2010). The G0/G1Switch Gene 2 Regulates Adipose Lipolysis through Association with Adipose Triglyceride Lipase. Cell Metab. *11*, 194–205. https://doi.org/10.1016/j.cmet.2010.02.003.

20. Cao, W., Daniel, K.W., Robidoux, J., Puigserver, P., Medvedev, A. V, Bai, X., Floering, L.M., Spiegelman, B.M., and Collins, S. (2004). p38 mitogen-activated protein kinase is the central regulator of cyclic AMP-dependent transcription of the brown fat uncoupling protein 1 gene. Mol. Cell. Biol. *24*, 3057–3067. https://doi.org/10.1128/MCB.24.7.3057.

21. Tabuchi, C., and Sul, H.S. (2021). Signaling Pathways Regulating Thermogenesis. Front. Endocrinol. (Lausanne). *12*. https://doi.org/10.3389/fendo.2021.595020.

22. Cannon, B. and Nedergaard, J. (2004). Brown Adipose Tissue: Function and Physiological Significance. Physiol. Rev. *84*, 277–359. https://doi.org/10.1152/physrev.00015.2003.

23. Schreiber, R., Diwoky, C., Schoiswohl, G., Feiler, U., Wongsiriroj, N., Abdellatif, M., Kolb, D., Hoeks, J., Kershaw, E.E., Sedej, S., et al. (2017). Cold-Induced Thermogenesis Depends on ATGL-Mediated Lipolysis in Cardiac Muscle, but Not Brown Adipose Tissue. Cell Metab. *26*, 753-763.e7. https://doi.org/10.1016/j.cmet.2017.09.004.

24. Shin, H., Ma, Y., Chanturiya, T., Cao, Q., Wang, Y., Kadegowda, A.K.G., Jackson, R., Rumore, D., Xue, B., Shi, H., et al. (2017). Lipolysis in brown adipocytes is not essential for cold-induced thermogenesis in mice. Cell Metab. *26*, 764–777. https://doi.org/10.1016/j.cmet.2017.09.002.

25. Cannon, B., and Nedergaard, J. (2017). What Ignites UCP1? Cell Metab. *26*, 697–698. https://doi.org/10.1016/j.cmet.2017.10.012.

26. Schoiswohl, G., Stefanovic-Racic, M., Menke, M.N., Wills, R.C., Surlow, B.A., Basantani, M.K., Sitnick, M.T., Cai, L., Yazbeck, C.F., Stolz, D.B., et al. (2015). Impact of reduced ATGL-mediated adipocyte lipolysis on obesity-associated insulin resistance and inflammation in male mice. Endocrinology *156*, 3610–3624. https://doi.org/10.1210/en.2015-1322.

27. Haemmerle, G., Moustafa, T., Woelkart, G., Buttner, S., Schmidt, A., van de Weijer, T.,

Hesselink, M., Jaeger, D., Kienesberger, P.C., Zierler, K., et al. (2011). ATGL-mediated fat catabolism regulates cardiac mitochondrial function via PPAR-alpha and PGC-1. Nat. Med. *17*, 1076–1085. https://doi.org/10.1038/nm.2439; 10.1038/nm.2439.

28. Fredrikson, G., Stralfors, P., Nilsson, N.O., and Belfrage, P. (1981). Hormone-sensitive lipase of rat adipose tissue. Purification and some properties. J. Biol. Chem. *256*, 6311–6320. https://doi.org/10.1016/0076-6879(81)71076-0.

29. Müller, T.D., Klingenspor, M., and Tschöp, M.H. Revisiting energy expenditure: how to correct mouse metabolic rate for body mass. https://doi.org/10.1038/s42255-021-00451-2.

30. Nedergaard, J., and Cannon, B. (2013). UCP1 mRNA does not produce heat. Biochim. Biophys. Acta - Mol. Cell Biol. Lipids *1831*, 943–949. https://doi.org/10.1016/j.bbalip.2013.01.009.

31. Sveidahl Johansen, O., Ma, T., Hansen, J.B., Markussen, L.K., Schreiber, R., Reverte-Salisa, L., Dong, H., Christensen, D.P., Sun, W., Gnad, T., et al. (2021). Lipolysis drives expression of the constitutively active receptor GPR3 to induce adipose thermogenesis. Cell *184*, 3502-3518.e33. https://doi.org/10.1016/j.cell.2021.04.037.

32. Nicholls, D ; Locke, R. (1984). Thermogenic Mechanisms in Brown Fat. Physiol. Rev. *64*, 3–64.

33. Li, Y., Fromme, T., Schweizer, S., Schottl, T., and Klingenspor, M. (2014). Taking control over intracellular fatty acid levels is essential for the analysis of thermogenic function in cultured primary brown and brite/beige adipocytes. EMBO Rep. *15*, 1069–1076. https://doi.org/10.15252/embr.201438775.

34. Zimmermann, R., Strauss, J.G., Haemmerle, G., Schoiswohl, G., Birner-Gruenberger, R., Riederer, M., Lass, A., Neuberger, G., Eisenhaber, F., Hermetter, A., et al. (2004). Fat Mobilization in Adipose Tissue Is Promoted by Adipose Triglyceride Lipase. Science (80-.). *306*, 1383–1386. https://doi.org/10.1126/science.1100747.

35. Ahmadian, M., Abbott, M.J., Tang, T., Hudak, C.S.S., Kim, Y., Bruss, M., Hellerstein, M.K., Lee, H.Y., Samuel, V.T., Shulman, G.I., et al. (2011). Desnutrin/ATGL is regulated by AMPK and is required for a brown adipose phenotype. Cell Metab. *13*, 739–748. https://doi.org/10.1016/j.cmet.2011.05.002.

36. Haemmerle, G., Lass, A., Zimmermann, R., Gorkiewicz, G., Meyer, C., Rozman, J., Heldmaier, G., Maier, R., Theussl, C., Eder, S., et al. (2006). Defective lipolysis and altered energy metabolism in mice lacking adipose triglyceride lipase. Science (80-.). *312*, 734–737. https://doi.org/10.1126/science.1123965.

37. Wu, J.W., Wang, S.P., Casavant, S., Moreau, A., Yang, G.S., and Mitchell, G.A. (2012). Fasting energy homeostasis in mice with adipose deficiency of desnutrin/adipose triglyceride lipase. Endocrinology *153*, 2198–2207. https://doi.org/10.1210/en.2011-1518.

38. Heim, T., and Hull, D. (1966). The blood flow and oxygen consumption of brown adipose tissue in the new-born rabbit. J. Physiol. *186*, 42–55. https://doi.org/10.1113/jphysiol.1966.sp008019.

39. Himms-Hagen, J., Cui, J., Danforth, E., Taatjes, D.J., Lang, S.S., Waters, B.L., and Claus, T.H. (1994). Effect of CL-316,243, a thermogenic beta 3-agonist, on energy balance and brown and white adipose tissues in rats. Am. J. Physiol. Integr. Comp. Physiol. *266*, R1371–R1382. https://doi.org/10.1152/ajpregu.1994.266.4.R1371.

40. Golozoubova, V. (2001). Only UCP1 can mediate adaptive nonshivering thermogenesis in the cold. FASEB J. *15*, 2048–2050. https://doi.org/10.1096/fj.00-0536fje.

41. Matthias, A., Ohlson, K.B.E., Fredriksson, J.M., Jacobsson, A., Nedergaard, J., and Cannon, B. (2000). Thermogenic Responses in Brown Fat Cells Are Fully UCP1-dependent. J. Biol. Chem. *275*, 25073–25081. https://doi.org/10.1074/jbc.M000547200.

42. Chitraju, C., Fischer, A.W., Farese, R. V., and Walther, T.C. (2020). Lipid Droplets in Brown Adipose Tissue Are Dispensable for Cold-Induced Thermogenesis. Cell Rep. *33*, 108348. https://doi.org/10.1016/j.celrep.2020.108348.

43. Shen, W.J., Yu, Z., Patel, S., Jue, D., Liu, L.F., and Kraemer, F.B. (2011). Hormone-sensitive lipase modulates adipose metabolism through PPARγ. Biochim. Biophys. Acta - Mol. Cell Biol. Lipids *1811*, 9–16. https://doi.org/10.1016/j.bbalip.2010.10.001.

44. Markussen, L.K., Rondini, E.A., Johansen, O.S., Madsen, J.G.S., Sustarsic, E.G., Marcher, A.-B., Hansen, J.B., Gerhart-Hines, Z., Granneman, J.G., and Mandrup, S. (2022). Lipolysis regulates major transcriptional programs in brown adipocytes. Nat. Commun. *13*, 3956.

https://doi.org/10.1038/S41467-022-31525-8.

45. Mottillo, E.P., Bloch, A.E., Leffs, T., and Granneman, J.G. (2012). Lipolytic products activate peroxisome proliferator-activated receptor (PPAR) α and δ in brown adipocytes to match fatty acid oxidation with supply. J. Biol. Chem. *287*, 25038–25048. https://doi.org/10.1074/jbc.M112.374041.

46. Susulic, V.S., Frederich, R.C., Lawitts, J., Tozzo, E., Kahn, B.B., Harper, M.-E., Himms-Hagen, J., Flier, J.S., and Lowell, B.B. (1995). Targeted Disruption of the β3-Adrenergic Receptor Gene. J. Biol. Chem. *270*, 29483–29492. https://doi.org/10.1074/jbc.270.49.29483.

47. Keipert, S., Kutschke, M., Ost, M., Schwarzmayr, T., van Schothorst, E.M., Lamp, D., Brachthäuser, L., Hamp, I., Mazibuko, S.E., Hartwig, S., et al. (2017). Long-Term Cold Adaptation Does Not Require FGF21 or UCP1. Cell Metab. *26*, 437-446.e5. https://doi.org/10.1016/j.cmet.2017.07.016.

48. Kazak, L., Chouchani, E.T., Stavrovskaya, I.G., Lu, G.Z., Jedrychowski, M.P., Egan, D.F., Kumari, M., Kong, X., Erickson, B.K., Szpyt, J., et al. (2017). UCP1 deficiency causes brown fat respiratory chain depletion and sensitizes mitochondria to calcium overload-induced dysfunction. Proc. Natl. Acad. Sci. *114*, 7981–7986. https://doi.org/10.1073/pnas.1705406114.

49. Wu, J.W., Preuss, C., Wang, S.P., Yang, H., Ji, B., Carter, G.W., Gladdy, R., Andelfinger, G., and Mitchell, G.A. (2017). Epistatic interaction between the lipase-encoding genes Pnpla2 and Lipe causes liposarcoma in mice. PLoS Genet. *13*, e1006716. https://doi.org/10.1371/journal.pgen.1006716.

50. Schulz, T.J., Huang, P., Huang, T.L., Xue, R., McDougall, L.E., Townsend, K.L., Cypess, A.M., Mishina, Y., Gussoni, E., and Tseng, Y.H. (2013). Brown-fat paucity due to impaired BMP signalling induces compensatory browning of white fat. Nature *495*, 379–383. https://doi.org/10.1038/nature11943.

51. Xie, H., Heier, C., Meng, X., Bakiri, L., Pototschnig, I., Tang, Z., Schauer, S., Baumgartner, V.J., Grabner, G.F., Schabbauer, G., et al. (2022). An immune-sympathetic neuron communication axis guides adipose tissue browning in cancer-associated cachexia. Proc. Natl. Acad. Sci. U. S. A. *119*, 1–12. https://doi.org/10.1073/pnas.2112840119.

52. Fabbiano, S., Suárez-Zamorano, N., Rigo, D., Veyrat-Durebex, C., Stevanovic Dokic, A., Colin, D.J., and Trajkovski, M. (2016). Caloric Restriction Leads to Browning of White Adipose Tissue through Type 2 Immune Signaling. Cell Metab. *24*, 434–446. https://doi.org/10.1016/j.cmet.2016.07.023.

53. Qiu, Y., Nguyen, K.D., Odegaard, J.I., Cui, X., Tian, X., Locksley, R.M., Palmiter, R.D., and Chawla, A. (2014). Eosinophils and type 2 cytokine signaling in macrophages orchestrate development of functional beige fat. Cell *157*, 1292–1308. https://doi.org/10.1016/j.cell.2014.03.066.

54. Liu, P., Ji, Y., Yuen, T., Rendina-Ruedy, E., Demambro, V.E., Dhawan, S., Abu-Amer, W., Izadmehr, S., Zhou, B., Shin, A.C., et al. (2017). Blocking FSH induces thermogenic adipose tissue and reduces body fat. Nature *546*, 107–112. https://doi.org/10.1038/nature22342.

55. Abe, I., Oguri, Y., Verkerke, A.R.P., Monteiro, L.B., Knuth, C.M., Auger, C., Qiu, Y., Westcott, G.P., Cinti, S., Shinoda, K., et al. (2022). Lipolysis-derived linoleic acid drives beige fat progenitor cell proliferation. Dev. Cell *57*, 2623-2637.e8. https://doi.org/10.1016/j.devcel.2022.11.007.

56. Preite, N.Z., Nascimento, B.P.P. do, Muller, C.R., Américo, A.L. V, Higa, T.S., Evangelista, F.S., Lancellotti, C.L., Henriques, F. dos S., Batista, M.L., Bianco, A.C., et al. (2016). Disruption of beta3 adrenergic receptor increases susceptibility to DIO in mouse. J. Endocrinol. *231*, 259–269. https://doi.org/10.1530/JOE-16-0199.

57. Oeckl, J., Janovska, P., Adamcova, K., Bardova, K., Brunner, S., Dieckmann, S., Ecker, J., Fromme, T., Funda, J., Gantert, T., et al. (2022). Loss of UCP1 function augments recruitment of futile lipid cycling for thermogenesis in murine brown fat. Mol. Metab. *61*. https://doi.org/10.1016/J.MOLMET.2022.101499.

58. Granneman, J.G., Burnazi, M., Zhu, Z., and Schwamb, L.A. (2003). White adipose tissue contributes to UCP1-independent thermogenesis. Am. J. Physiol. - Endocrinol. Metab. *285*, E1230–E1236. https://doi.org/10.1152/ajpendo.00197.2003.

59. Ukropec, J., Anunciado, R.P., Ravussin, Y., Hulver, M.W., and Kozak, L.P. (2006). UCP1-independent thermogenesis in white adipose tissue of cold-acclimated Ucp1-/-mice. J. Biol. Chem. *281*, 31894–31908. https://doi.org/10.1074/jbc.M606114200.

60. Rahbani, J.F., Bunk, J., Lagarde, D., Samborska, B., Roesler, A., Xiao, H., Shaw, A., Kaiser, Z., Braun, J.L., Geromella, M.S., et al. (2024). Parallel control of cold-triggered adipocyte thermogenesis by UCP1 and CKB. Cell Metab., 1–15. https://doi.org/10.1016/j.cmet.2024.01.001.

61. Ikeda, K., Kang, Q., Yoneshiro, T., Camporez, J.P., Maki, H., Homma, M., Shinoda, K., Chen, Y., Lu, X., Maretich, P., et al. (2017). UCP1-independent signaling involving SERCA2bmediated calcium cycling regulates beige fat thermogenesis and systemic glucose homeostasis. Nat. Med. *23*, 1454–1465. https://doi.org/10.1038/nm.4429.

62. Mayer, N., Schweiger, M., Romauch, M., Grabner, G.F., Eichmann, T.O., Fuchs, E., Ivkovic, J., Heier, C., Mrak, I., Lass, A., et al. (2013). Development of small-molecule inhibitors targeting adipose triglyceride lipase. Nat. Chem. Biol. *9*, 785–787. https://doi.org/10.1038/nchembio.1359.

63. Sitnick, M.T., Basantani, M.K., Cai, L., Schoiswohl, G., Yazbeck, C.F., Distefano, G., Ritov, V., DeLany, J.P., Schreiber, R., Stolz, D.B., et al. (2013). Skeletal muscle triacylglycerol hydrolysis does not influence metabolic complications of obesity. Diabetes *62*, 3350–3361. https://doi.org/10.2337/db13-0500.

64. Haemmerle, G., Zimmermann, R., Hayn, M., Theussl, C., Waeg, G., Wagner, E., Sattler, W., Magin, T.M., Wagner, E.F., and Zechner, R. (2002). Hormone-sensitive lipase deficiency in mice causes diglyceride accumulation in adipose tissue, muscle, and testis. J. Biol. Chem. *277*, 4806–4815. https://doi.org/10.1074/jbc.M110355200.

65. Rosenwald, M., Perdikari, A., Rülicke, T., and Wolfrum, C. (2013). Bi-directional interconversion of brite and white adipocytes. Nat. Cell Biol. *15*, 659–667. https://doi.org/10.1038/ncb2740.

66. Eguchi, J., Wang, X., Yu, S., Kershaw, E.E., Chiu, P.C., Dushay, J., Estall, J.L., Klein, U., Maratos-Flier, E., and Rosen, E.D. (2011). Transcriptional control of adipose lipid handling by IRF4. Cell Metab. *13*, 249–259. https://doi.org/10.1016/j.cmet.2011.02.005.

67. Pajed, L., Taschler, U., Tilp, A., Hofer, P., Kotzbeck, P., Kolleritsch, S., Radner, F.P., Pototschnig, I., Wagner, C., Schratter, M., et al. (2021). Advanced lipodystrophy reverses fatty liver in mice lacking adipocyte hormone-sensitive lipase. Commun. Biol. *4*, 323.

https://doi.org/10.1038/S42003-021-01858-Z.

68. du Sert, N.P., Hurst, V., Ahluwalia, A., Alam, S., Avey, M.T., Baker, M., Browne, W.J., Clark, A., Cuthill, I.C., Dirnagl, U., et al. (2020). The ARRIVE guidelines 2.0: Updated guidelines for reporting animal research. PLoS Biol. *18*. https://doi.org/10.1371/JOURNAL.PBIO.3000410.

69. Tschöp, M.H., Speakman, J.R., Arch, J.R.S., Auwerx, J., Brüning, J.C., Chan, L., Eckel, R.H., Farese, R. V., Galgani, J.E., Hambly, C., et al. (2012). A guide to analysis of mouse energy metabolism. Nat. Methods *9*, 57–63. https://doi.org/10.1038/nmeth.1806.

70. Fischer, A.W., Hoefig, C.S., Abreu-Vieira, G., de Jong, J.M.A., Petrovic, N., Mittag, J., Cannon, B., and Nedergaard, J. (2016). Leptin Raises Defended Body Temperature without Activating Thermogenesis. Cell Rep. *14*, 1621–1631. https://doi.org/10.1016/j.celrep.2016.01.041.

71. Virtue, S., and Vidal-Puig, A. (2013). Assessment of brown adipose tissue function. Front. Physiol. *4*, 128. https://doi.org/10.3389/fphys.2013.00128.

72. Ying, Z., Boon, M.R., Coskun, T., Kooijman, S., and Rensen, P.C.N. (2021). A simplified procedure to trace triglyceride-rich lipoprotein metabolism in vivo. Physiol. Rep. *9*, 1–8. https://doi.org/10.14814/phy2.14820.

73. Fischer, A.W., Jaeckstein, M.Y., Gottschling, K., Heine, M., Sass, F., Mangels, N., Schlein, C., Worthmann, A., Bruns, O.T., Yuan, Y., et al. (2021). Lysosomal lipoprotein processing in endothelial cells stimulates adipose tissue thermogenic adaptation. Cell Metab. *33*, 547-564.e7. https://doi.org/10.1016/J.CMET.2020.12.001.

74. Kai, H., and Huiyun, F. (2008). A path to democracy: In search of China's democratization model. Asian Perspect. *32*, 139–169. https://doi.org/10.1006/meth.2001.1262.

75. Wessel, D., and Flügge, U.I. (1984). A method for the quantitative recovery of protein in dilute solution in the presence of detergents and lipids. Anal. Biochem. *138*, 141–143. https://doi.org/10.1016/0003-2697(84)90782-6.

76. Schweiger, M., Eichmann, T.O., Taschler, U., Zimmermann, R., Zechner, R., and Lass, A. (2014). Measurement of lipolysis. In Methods in Enzymology, pp. 171–193. https://doi.org/10.1016/B978-0-12-800280-3.00010-4.

Figures and figure legends

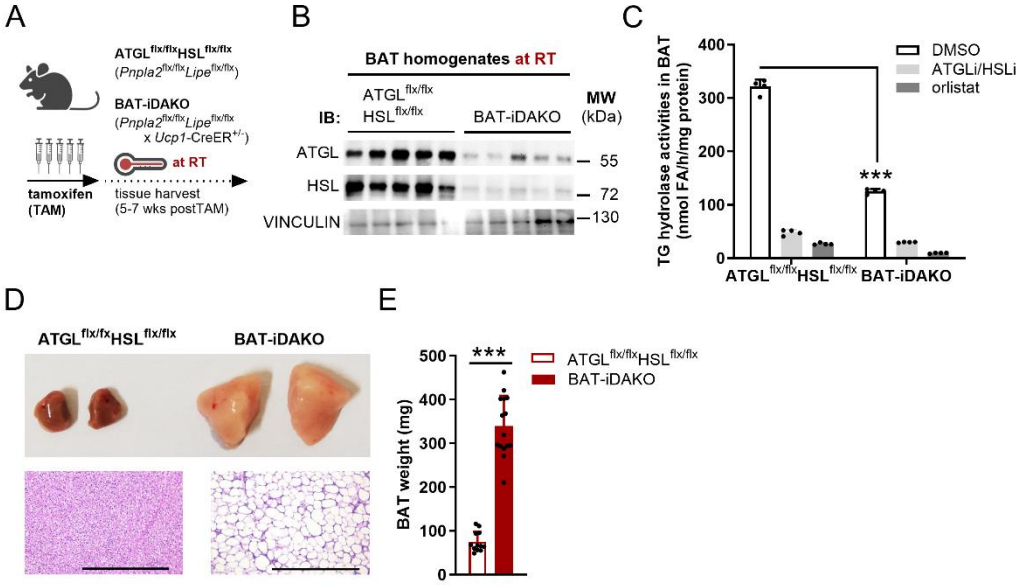

Figure 1. Genetic loss of ATGL and HSL in brown adipocytes causes BAT hypertrophy. Brown-adipocyte specific ATGL and HSL knockout mice (BAT-iDAKO) were generated by crossing *Pnpla2*$^{flx/flx}$*Lipe*$^{flx/flx}$ with *Ucp1*-CreER$^{+/-}$ mice. Gene deletion was induced in adult male mice by intragastric gavage of tamoxifen (TAM) for 5 subsequent days.

(A) Schematic presentation of mouse model studied and tamoxifen treatment.

(B) Immunoblot (IB) analyses from total BAT homogenates. Delipidated volume equivalents of 0.25% from total BAT were loaded per lane.

(C) TG hydrolase activities were determined in a pooled fraction of fat-free infranatants from BAT homogenates (n = 7) using a radiolabeled triolein substrate emulsified with phospholipids. Enzymatic activities were determined in the absence or presence of inhibitors specific for ATGL (ATGLi) or HSL (HSLi) or the non-specific serine hydrolase inhibitor orlistat. Technical replicates are shown.

(D) Morphology and histology (upper and lower graph). Bar graph is 500 µm.

(E) BAT weights. n = 12-15.

Data are means + SD from male mice housed at ambient room temperature of 21-23 °C and 6-14 weeks post-TAM. Statistical analyses were performed using student's *t*-test. ***, p<0.001.

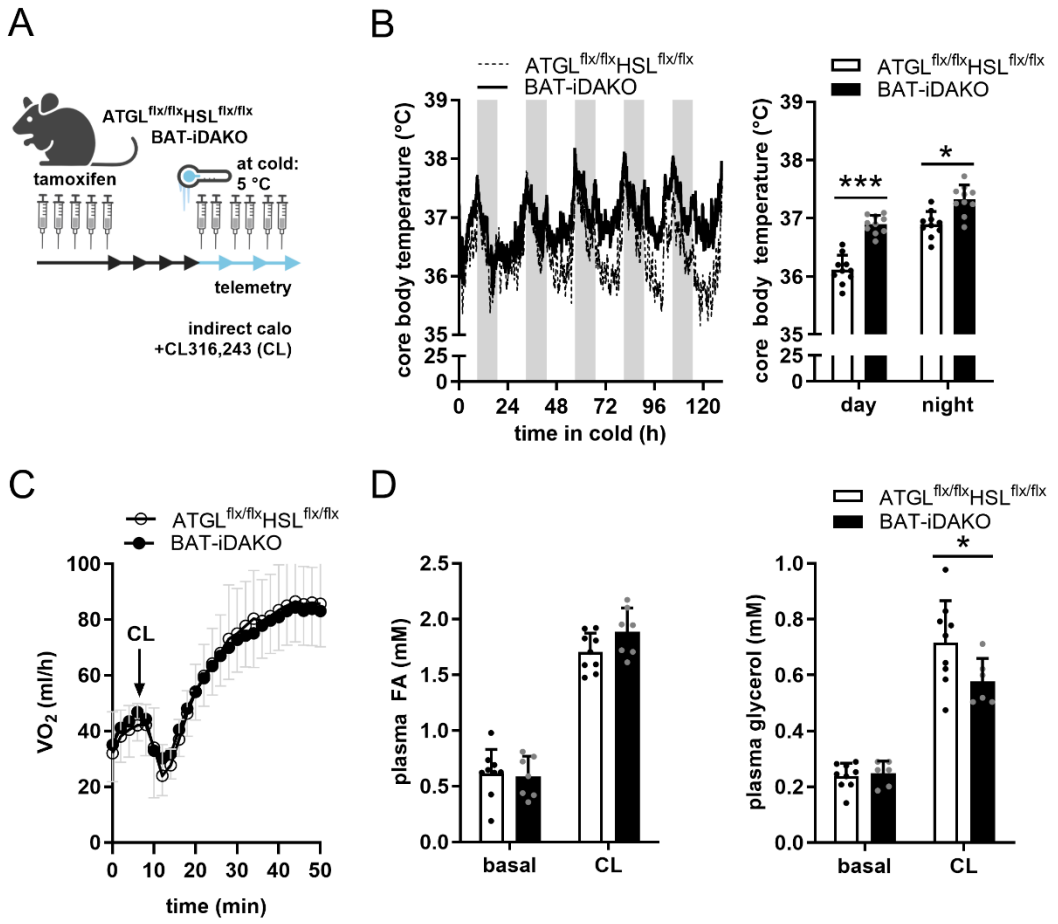

Figure 2. BAT-iDAKO mice exhibit increased core body temperature and intact NST upon cold adaptation.

(A) Schematic presentation of mouse model studied, tamoxifen treatment, and experimental settings. Blue thermometer indicates cold exposure at 5 °C. Arrows indicate weeks.

(B) Time-course (left) and mean (right) of core body temperature at 5 °C (n = 10) and

(C) Oxygen consumption (VO_2) during unstimulated and upon CL316,243 (CL) injection in pentobarbital-anesthetized mice upon cold adaptation (n = 12-13). VO_2 was analyzed at an ambient temperature of 28-30 °C.

(D) Plasma FA and glycerol levels during unstimulated (basal) and upon CL (n = 7-9).

Mice were implanted with telemetry transmitters and exposed to 5 °C for ≥3-weeks. Data are means + SD (except for time-course in B showing mean only) from male mice aged 19-28 weeks and 7-11 weeks post-TAM. Non-shaded and grey shaded areas represent day and night, respectively. Statistical analyses were performed using student's *t*-test. *, $p<0.05$, and ***, $p<0.001$.

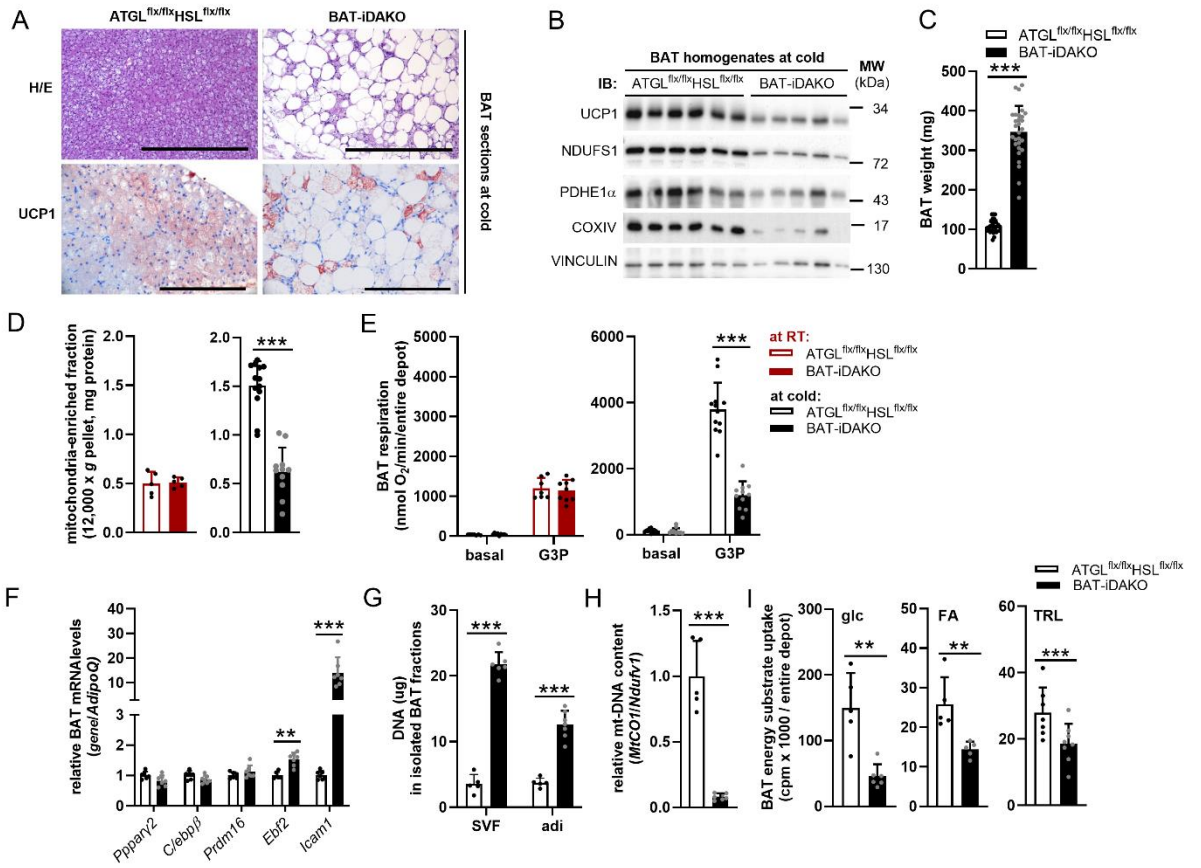

Figure 3. BAT-iDAKO mice have impaired BAT thermogenic capacity upon cold adaptation.

(A) Histology (H/E stain, top, bar graph is 500 µm) and UCP1 immunohistochemistry (bottom, bar graph is 200 µm) in BAT sections of cold adapted ATGL$^{flx/flx}$HSL$^{flx/flx}$ and BAT-iDAKO mice.

(B) Immunoblot (IB) of BAT homogenates upon cold adaptation. Delipidated volume equivalents of 0.25% of total BAT were loaded per lane.

(C) BAT weights (n = 29).

(D) Protein content in the mitochondria-enriched fraction (12,000 x *g* pellet) isolated from BAT from mice housed at room temperature (RT, (n=5) and upon cold adaptation (n = 11-13).

(E) Respiration using the substrate glycerol-3-P (G3P) in BAT homogenates from mice housed at RT (n=7-9) and upon cold adaptation (n = 11-12).

(F) Gene expression in BAT (n = 6-7).

(G) DNA content in the isolated stromavascular fractions (SVF) and brown adipocytes (adi) from whole BAT depots (n = 5-7).

(H) Relative mitochondrial content in isolated brown adipocytes (n = 5-7).

(I) Energy substrate uptake in BAT using ^{3}H-2-deoxyglucose (glucose, n = 5-6), ^{14}C-*R*-2-bromo palmitic acid (FA, n=5), and ^{3}H-TG-rich lipoproteins (TRL, n = 7-8) upon cold adaptation.

RT-housed male mice were 17-25 weeks of age and 6-8 weeks post TAM. Cold-adapted male mice were 16-24 weeks of age and 6-11 weeks post-TAM that were cold-adapted at 5 °C for ≥3 weeks. Data are means + SD. Statistical analyses were performed using student's *t*-test. **, p<0.01 and ***, p<0.001.

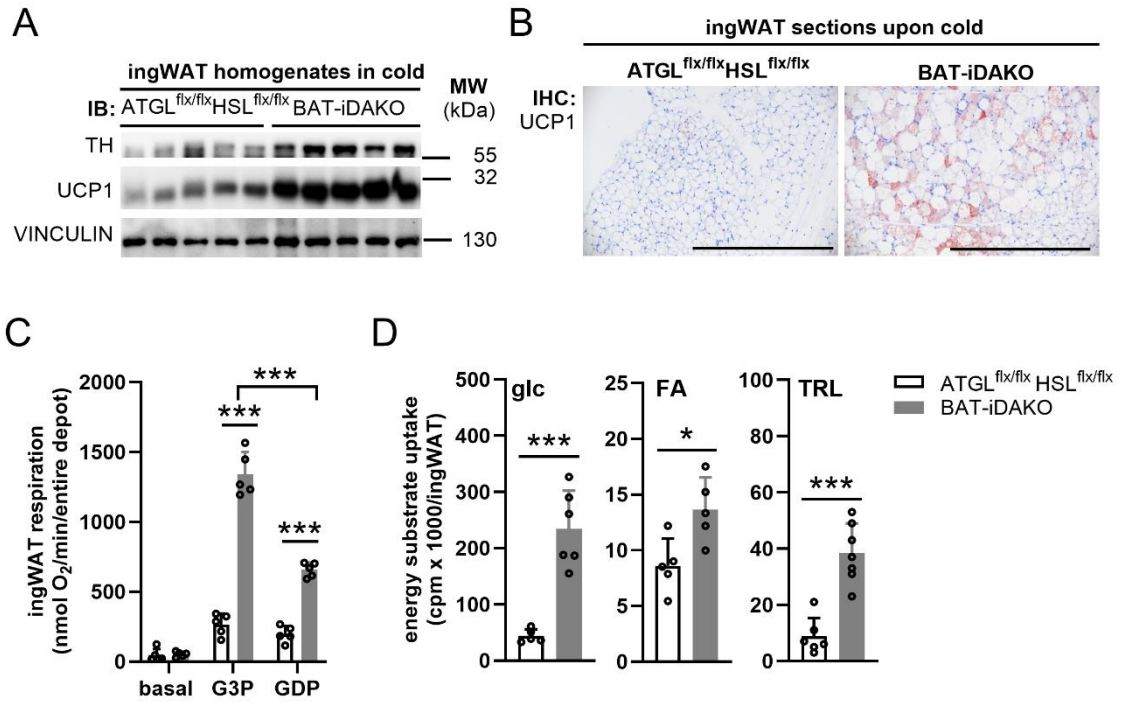

Figure 4. Inguinal white adipose tissue (ingWAT) is browned in BAT-iDAKO during cold.

(A) Immunoblot (IB) of ingWAT homogenates upon cold adaptation. Volume equivalents of 0.25% of total ingWAT were loaded per lane.

(B) Immunohistochemistry (IHC) from ingWAT sections. Bar graph = 500 µm.

(C) Respiration in ingWAT homogenates upon cold adaptation using the substrate glycerol-3-P (G3P) and guanosine-5'-diphosphate (GDP) for UCP1 inhibition (n = 5).

(D) Energy substrate uptake in ingWAT upon cold adaptation using ^{3}H-2-deoxyglucose (glucose, n = 6), 14C-*R*-2-bromo palmitic acid (FA, n=5), and ^{3}H-TG rich lipoproteins (TRL, n = 6-7).

Male mice of 16-24 weeks of age and 6-8 weeks post-TAM were exposed to 5 °C for ≥3-weeks. Data are means + SD. Statistical analyses were performed using student's *t*-test. *, p<0.05 and ***, p<0.001.

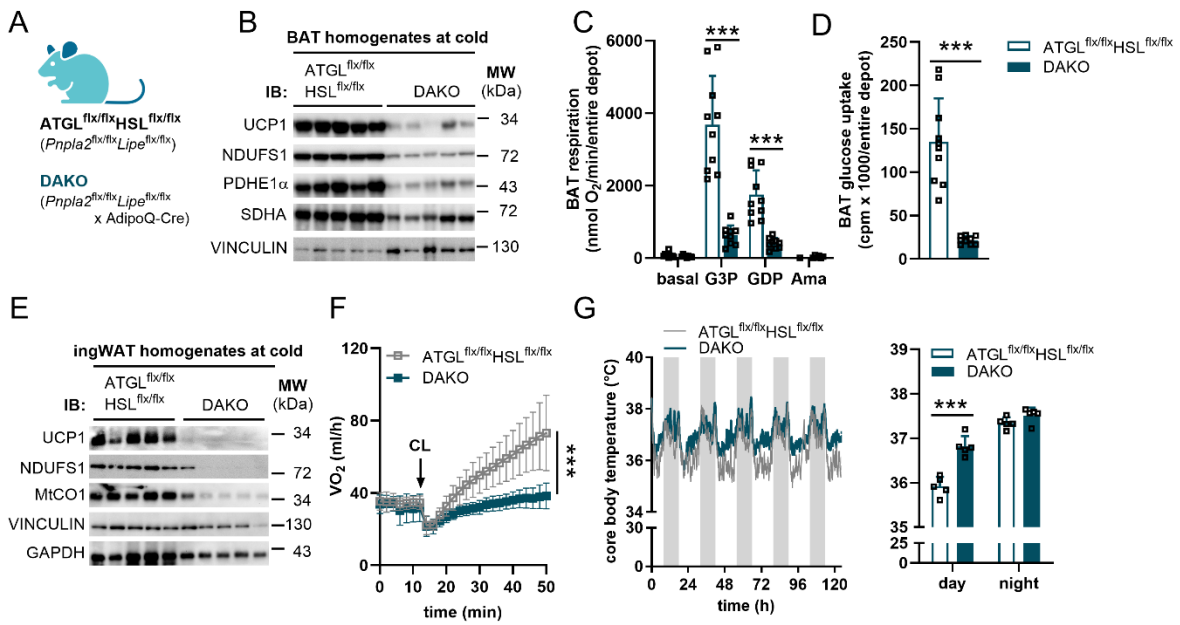

Figure 5. Genetic loss of ATGL and HSL in all adipocytes (DAKO) impairs NST in cold.

(A) Mouse model studied.

(B) Immunoblot (IB) of BAT homogenates. Volume equivalents of 0.25% of total BAT were loaded per lane.

(C) Respiration in BAT homogenates (n = 9-10).

(D) BAT glucose uptake using ^{3}H-2-deoxyglucose (n = 9-10).

(E) Immunoblot (IB) of ingWAT homogenates (5 µg tissue protein per lane).

(F) Oxygen consumption (VO_2) during unstimulated and upon CL316,243 (CL) injection in pentobarbital-anaesthetized mice upon cold adaptation (n = 7-8). VO_2 was analyzed at an ambient temperature of 28-30 °C.

(G) Core body temperature using implanted telemetry transmitters. Time-course (left) and mean only (right) at 5 °C (n = 5). Non-shaded and grey shaded areas represent day and night, respectively.

Male mice aged 14-17 weeks of age and upon cold adaptation at 5 °C for ≥3 weeks were studied. Data are means + SD except otherwise stated. Statistical analyses were performed using student's *t*-test. ***, p<0.001.